Electronic Supplementary Material (ESI) for Nanoscale.

ARTICLE - Supplement

Tailoring magnetic anisotropy by graphene-induced selective skyhook effect on 4*f*-metals

Received 16th March 2022,
Accepted 09th May 2022

DOI: 10.1039/D2NR01458K

Alexander Herman,*[a] Stefan Kraus,[b] Shigeru Tsukamoto,[c] Lea Kämmerer,[a] Vasile Caciuc,[c] Tobias Lojewski,[a] Damian Günzing,[a] Jan Dreiser,[d] Bernard Delley,[d] Katharina Ollefs,[a] Thomas Michely,[b] Nicolae Atodiresei †[c] and Heiko Wende [a]

From macroscopic heavy-duty permanent magnets to nanodevices, the precise control of the magnetic properties in rare-earth metals is crucial for many applications used in our daily life. Therefore, a detailed understanding and manipulation of the 4*f*-metals magnetic properties are key to further boosting the functionalization and efficiency of future applications. We present a proof-of-concept approach consisting of a dysprosium-iridium surface alloy in which graphene adsorption allows us to tailor its magnetic properties. By adsorbing graphene onto a long-range ordered two-dimensional dysprosium-iridium surface alloy, the magnetic 4*f*-metal atoms are selectively lifted from the surface alloy. This selective skyhook effect introduces a giant magnetic anisotropy in dysprosium atoms as a result of manipulating its geometrical structure within the surface alloy. Introducing and proving this concept by our combined theoretical and experimental approach provides an easy and unambiguous understanding of its underlying mechanism. Our study sets the ground for an alternative path on how to modify the crystal field around 4*f*-atoms and therefore their magnetic anisotropies.

Supplement

Synthesis and structure determination

In order to understand how the system changes during annealing, a comparison of STM topographs after deposition and after additional annealing is helpful. In Supp. Fig. 1 a, the STM topography taken at 20 K shows the sample after the room temperature deposition of 0.125 $\mathrm{ML_{Ir}}$ on Ir(111). A frozen Dy adatom gas coexists with Dy islands. The apparent island height indicated in the profile in Supp. Fig. 1 c, is about 2.8 Å, whereas the single atoms have an apparent height of about 2 Å. The apparent height of the islands corresponds to the spacing of dense-packed layers in Dy bulk (2.82 Å). While imaging of the unannealed sample was not possible due to the high mobility of the Dy adatom gas phase, the STM topograph of the annealed sample in Supp. Fig 1 b was taken at room temperature and no mobility of the atoms has been detected. Now nearly no single atoms show up and the apparent height of the Dy atoms has strongly decreased. The islands, now ordered in a (2x2) superstructure with respect to the Ir surface, have an apparent height of about 0.5 Å as visible in the profile displayed in Supp. Fig. 1 d. In addition, defects in the Ir surface are visible as dark holes, mostly next to the Dy islands, which we assign to stress due to the incorporation of the Dy atoms.

By combining all this information, the stronger binding, the lower apparent height, the ordering with respect to the Ir lattice, and the increased defect density, we conclude on surface alloy formation, in which the Dy atoms replace an Ir atom in the surface layer, leading to a (2x2) superstructure.

Sum-rule analysis

By utilizing the circular dichroic signal of the XANES, one can determine the magnetism element specifically. In addition, spin and orbital magnetism can be separated. The analysis of the XMCD signal is based on the sum rules, introduced by Thole and Carra (1).

For the $M_{5,4}$ edges, where one excites the electron from the 3*d* core level to the 4*f* level of the atoms, the sum-rules are given as:

$$\langle L_Z \rangle = \frac{2\,(p+q)}{r} n_h$$

Hereby, $\langle L_Z \rangle$ is the expectation value of the angular momentum along the quantisation axis Z, *p* the integral of the XMCD signal of the M_5 edge, *q* the integral of the XMCD signal of the M_4 edge, and r the integral of the XANES signal of both edges. n_h is the number of holes in the valence shell, in our case $n_h = 5$. For the effective spin magnetism, the expectation value is given as

$$\langle S_Z^{eff} \rangle \equiv \langle S_Z \rangle + 3\langle T_Z \rangle = \frac{2p\ -\ 3q}{2r} n_h$$

---

[a] Faculty of Physics and Center for Nanointegration Duisburg-Essen (CENIDE), University of Duisburg-Essen, Lotharstr. 1, 47058 Duisburg, Germany.
[b] II. Physikalisches Institut, Universität zu Köln, Zülpicher Straße 77, 50937 Köln, Germany.
[c] Peter Grünberg Institute and Institute for Advanced Simulation, Forschungszentrum Jülich, 52428 Jülich, Germany.
[d] Swiss Light Source (SLS), Paul Scherrer Institute (PSI), CH-5232 Villigen PSI, Switzerland.

† Corresponding author for DFT calculations.

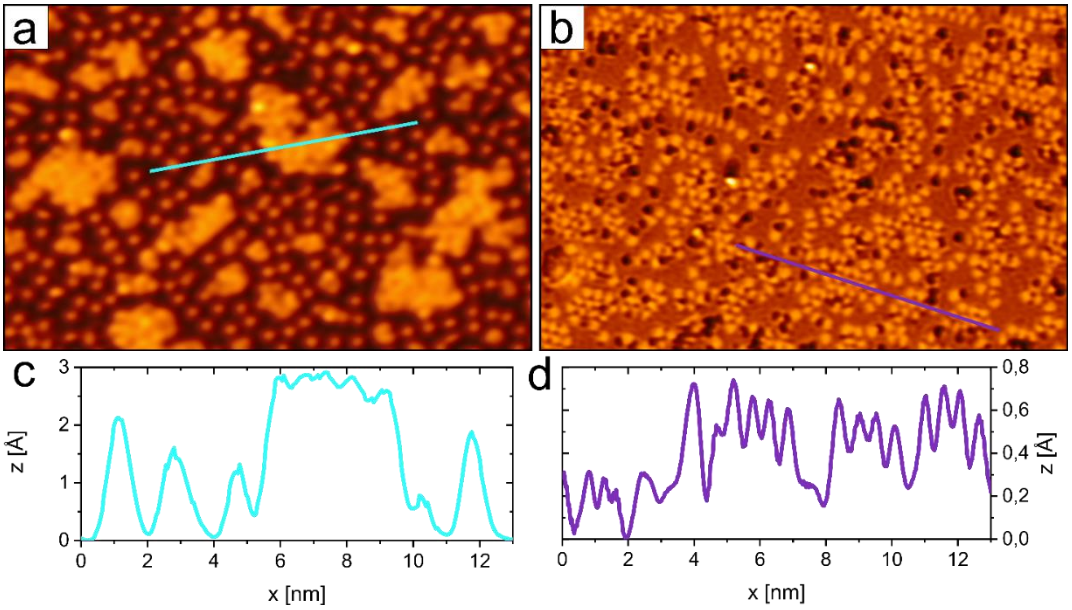

Supp. Fig. 1: Synthesis of (2x2) superstructure – STM

a STM topograph after the deposition of 0.125 ML$_{\text{Ir}}$ Dy on Ir(111) (compare Fig. 1 **e**) (25.3 nm x 16.6 nm). The turquoise line indicates the profile in **c**. **b** STM topograph after annealing the sample in **a** to 1480 K (compare Fig. 1 **h**) (25.3 nm x 16.6 nm). The purple line shows the profile in **d**. The tunnelling parameters used are **a** I = 0.15 nA, U = -2.11 V and **b** I = 1.1 nA, U = -1.05 V

with the dipolar term $\langle T_Z\rangle$. This dipolar term cannot be measured easily by XMCD but using the relationship of $\frac{\langle S_Z\rangle}{\langle L_Z\rangle}$ as given in Collins et al. (2) enables the derivation of $\langle T_Z\rangle$ in terms of q and r such that $\langle T_Z\rangle = \frac{-5q}{6r} n_h$. Another option to get the value of $\langle T_Z\rangle$ is to use multiplet calculations to simulate the spectra. In our case, the difference between both methods is negligible and in the range of the error.

The magnetic moments given in the manuscript are given as $\mu_l = -\langle L_Z\rangle\, \mu_B$ and $\mu_s = -2\,\langle S_Z\rangle\, \mu_B$. The error is approximated by 15% of the calculated value.

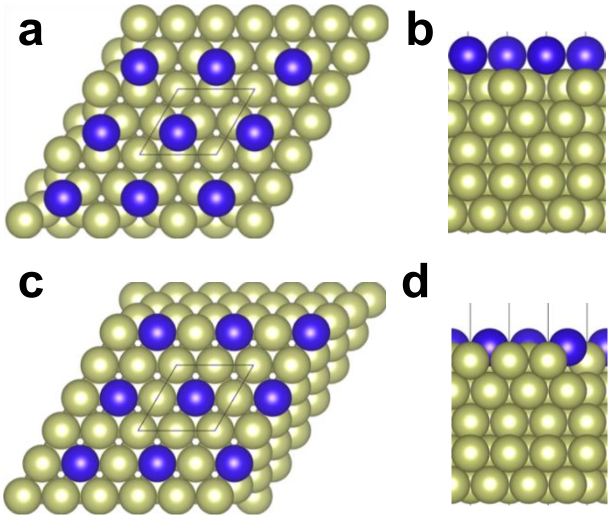

Supp. Fig. 2: 2x2 superstructure without Gr

a Top and **b** side views of the ground state structures for a Dy atom adsorbed above Ir(111) surface and **c, d** embedded within the surface layer of the Ir(111) substrate. The calculated in-plane (2x2) unit cell is indicated by the black lines. With respect to the first Ir layer, when a Dy atom is adsorbed above the surface it is located at 2.055 Å and just 0.667 Å when it is embedded within the surface layer.

DFT calculations – structural comparison, projected density of states, and magnetic properties

Supp. Fig. 2 and 3 display the systems compared, each one with Dy adsorbed on the Ir (a,b) and the Dy incorporated (c,d). As discussed in the main text, the embedded systems are energetically more favourable in both cases.

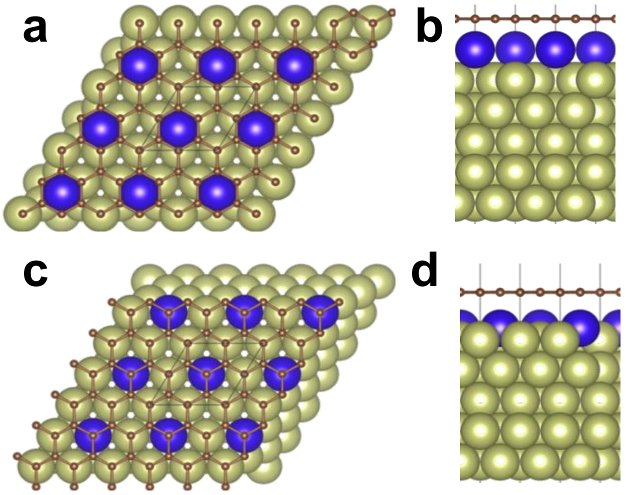

Supp. Fig. 3: 2x2 superstructure with Gr

a Top and **b** side views of the ground state geometries for a Dy atom intercalated between Gr and Ir(111) surface and **c, d** Gr adsorbed onto the surface alloy formed by Dy atoms embedded within a (2x2) in-plane unit cell of the first surface layer of the Ir(111) substrate. With respect to the first Ir layer, when a Dy atom is adsorbed above the surface it is located at 2.251 Å and just 0.826 Å when it is embedded within the surface layer. **a, b** Gr is 4.508 Å away from Ir substrate and 2.257 Å above the intercalated Dy layer. **c, d** is 3.448 Å away from Ir substrate and 2.622 Å above Dy embedded into the Ir(111) surface.

The exact values are given in Supp. Table 1.

Adsorption energies in eV			
System	Dy to Ir(111) [$E_{Dy/Ir(111)}$ – (E_{Dy} + $E_{Ir(111)}$)]	Dy to Gr & Ir(111) [$E_{Gr/Dy/Ir(111)}$ – (E_{Dy} + $E_{Ir(111)}$ + E_{Gr})]	Gr to substrate [$E_{Gr/Dy/Ir(111)}$ – (E_{Gr} + $E_{Dy/Ir(111)}$)]
on top/ intercalated	-8.209	-9.995	-1.792
embedded	-10.911	-11.884	-0.9731

Supp. Table 1: The adsorption (binding) energies are calculated as the difference between the total energies of the systems and the sum of the isolated parts.

For the evaluation of the graphene-covered surface alloy, different configurations have to be considered due to the inconsumable lattices of Gr and Ir. The three different configurations are presented in Supp. Fig. 4.

The three different configurations show qualitatively the same behaviour. The total energy is lowest for the atop position of the carbon, nearly similar to the situation where the hexagon is situated above the Dy (+0.063 eV). The most unfavoured position is below a carbon-carbon bond. Here the total energy is 0.558 eV higher than for the atop position, but still far below the intercalation case presented in Supp. Fig 3 a and b.

Supp. Fig. 5 displays the spin-polarized projected density of states. The projection of the total charge density (effective magnetic moment) onto a sphere around the Dy atom onto the s, p, d, and f atomic-like orbitals leads to the following quantities: 0.26 (+0.02 μ_B) in s, 1.03 (+0.07 μ_B) in d and 9.26 (+5.03 μ_B) in f for embedded Dy/Ir(111) system and 0.24 (+0.02 μ_B) in s, 1.01 (+0.06 μ_B) in d and 9.24 (+5.11 μ_B) in f for graphene-covered Dy/Ir(111) substrate, respectively.

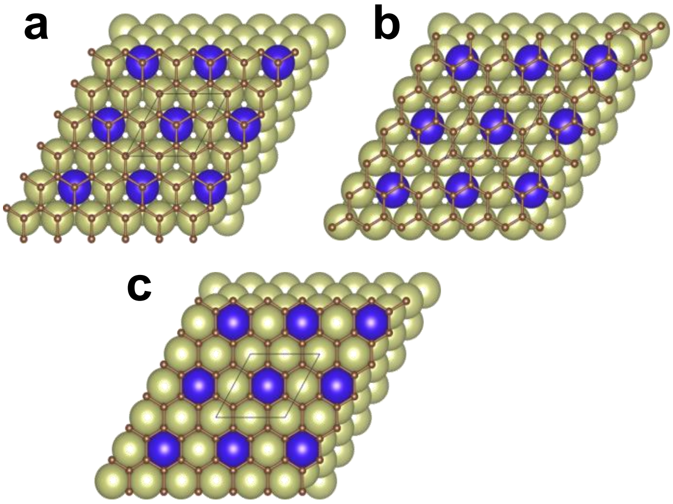

Supp. Fig. 4: Variation of the relative Gr position

The three different configurations used in the calculations. The carbon atoms are placed **a** atop, **b** with the bond, and **c** with the hexagon relative to the Dy atoms.

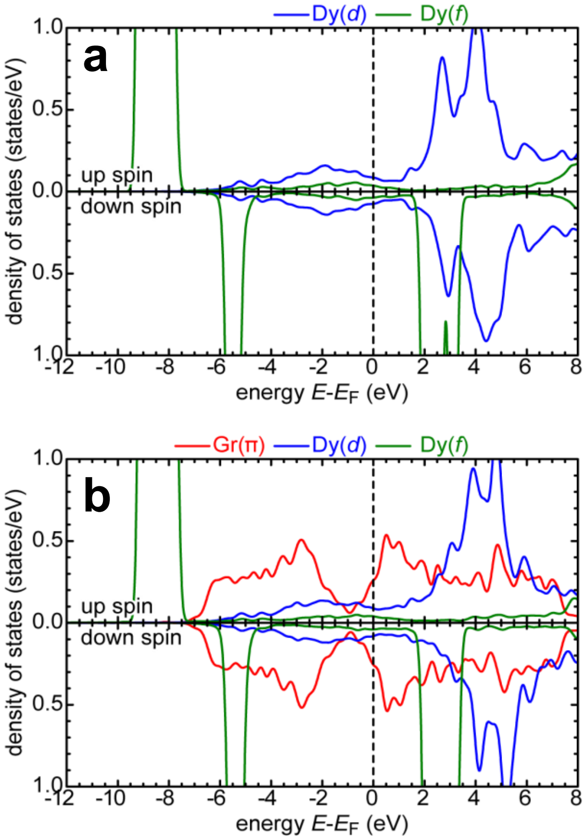

Supp. Fig. 5: Spin-polarized projected density of states

The spin-polarized projected density of states for the **a** clean and **b** graphene-covered embedded Dy/Ir(111) substrate. The Gr π-like orbitals are plotted in red colour and refer to the projection of the electronic states of the hybrid system into the p_z-like atomic orbitals of the C atoms building the Gr layer. The projection of the electronic states of the combined system onto the Dy atomic-like orbitals are plotted with a blue line on 5*d*-states while the 4*f*-states are indicated by the green line.

Besides the hybridization, noted in the main manuscript, we also stress that after its adsorption onto the Dy/Ir(111) substrate Gr becomes n-doped. This can be visualized in Supp. Fig. 5 b (red line) since the states associated with a Dirac-like feature appear -0.75 eV below Fermi level. This is slightly below the value estimated by the XPS measurement presented in Supp. Fig. 7.

In order to understand how the interaction of Gr with the Dy atoms embedded into the Ir surface layer influences their magnetic properties, we performed theoretical calculations for different magnetic configurations as illustrated in Fig. 6. For the clean Dy/Ir(111) substrate the energy difference between ferromagnetic and antiferromagnetic configurations amounts to -0.073 eV (i.e. -18 meV per Dy atom). However, when adsorbing Gr on the Dy/Ir(111) surface this energy difference is drastically increased to -1.985 eV (i.e. -496 meV per Dy atom). In simple words, by adsorbing Gr onto the Dy embedded within the Ir surface layer, the ferromagnetic interaction between the

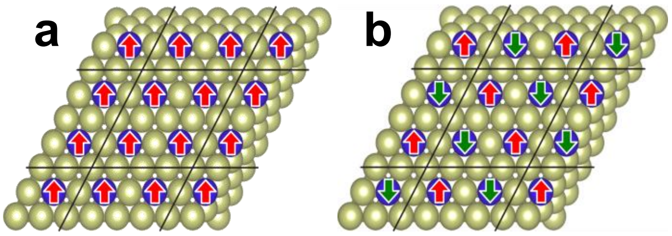

Supp. Fig. 6: Ferro- and Antiferromagnetic configurations

The calculated ferromagnetic **a** and the antiferromagnetic **b** configurations of the Dy atoms in a (4x4) in-plane surface unit cell.

magnetic Dy atoms is enhanced. To the best of our knowledge, this effect has not been reported yet for 4*f*-metals, although similar behaviour was theoretically and experimentally observed when Gr or molecular π-like conjugated systems interact with 3*d*-metals (3-7).

In the simplest classical Heisenberg model, the corresponding Heisenberg Hamiltonian is given by

$$\hat{H}_{Heisenberg} = -\sum_{\langle ij\rangle} J\mathbf{S}_i \cdot \mathbf{S}_j$$

where J represents the magnetic exchange constant and $S_{i,j}$ are the spin moments of the interacting atoms. This implies that for our specific calculated magnetic structures, using the simplest model, the energy difference between ferromagnetic (FM) and antiferromagnetic (AFM) configurations can be written as:

$$E_{FM}\text{-}E_{AFM} = (6*J*M*M) - (-4*J*M*M+2*J*M*M) = 8*J*M*M\ ,$$

where M represents the spin moment of Dy atom.

In the case of a clean Dy/Ir(111) surface, this energy difference is E_{FM}-E_{AFM} = 73 meV = 8*J_{clean}*5*5 while for graphene-covered Dy/Ir(111) substrate this is E_{FM}-E_{AFM} = 1985 meV = 8*$J_{covered}$*5*5 In consequence, for the Gr/Dy/Ir(111) system the magnetic exchange interaction $J_{covered}$ amounts to 9.93 meV/μ_B that is largely increased as compared to the one of the clean Dy/Ir(111) systems where J_{clean} amounts to 0.36 meV/μ_B. It is important to note, that the handling of large orbital moments, especially for 4*f*-metals, is intensively discussed and a crucial point in DFT calculations. In experiment, a significant deviation from $\mu_l = \mu_s$ for Dy in a $4f^9$ configuration has not been observed. To tackle this issue, we use our combined DFT-multiplet approach, as described in the main manuscript.

X-ray photoemission spectroscopy

X-ray photoemission spectroscopy (XPS) reveals the binding energies of the electrons close to the surface. Due to the different binding energies, it is also an element-specific probe. The experimental data shown in Supp. Fig. 7 has been acquired in a UHV-XPS set-up using an Al-K_α x-ray source as excitation. Supp. Fig. 7 a depicts the low energy XPS spectra of Gr on Ir(111) and our graphene-covered surface alloy. In direct comparison, the spectra are very similar, only one additional peak appears for the graphene-covered surface alloy, the Dy $4d_{3/2,5/2}$ states at 153.6 eV. Another interesting feature is the shift in the C 1s peak, as it hints at the doping level of the Gr. The zoom-in on the C 1s peak with subtracted background in Supp. Fig. 7 b clearly shows the shift of about 0.9 eV between the C 1s peak of both spectra. As already expected in the DFT calculation, this shift reveals negative doping of the Gr. By using the relation presented in Schröder et al. (8) this results in a doping level of about -1.1 eV.

X-ray linear dichroism and deviation from Hund's rule

X-ray absorption spectroscopy is not only able to observe the electron occupancy, the crystal field, and the magnetism of a system element specifically but has also the ability to detect charge anisotropy of the measured shell. To detect charge anisotropies, which can provide additional information about

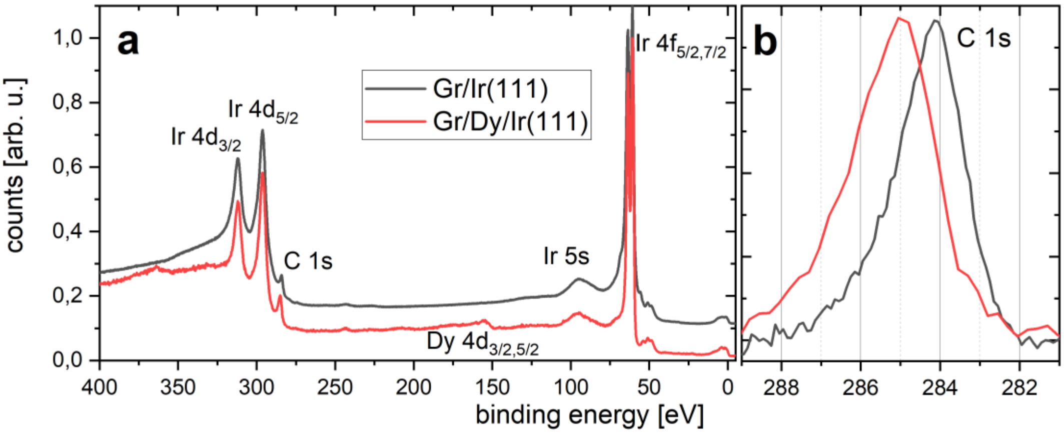

Supp. Fig. 7: Gr doping and electronic binding energies

a Experimental XPS binding energies for Gr/Ir(111) and the graphene-covered (2x2) Dy surface alloy. The Gr/Ir(111) spectrum is shifted up for better visibility. The peaks are assigned to their respective core levels. **b** Close up on the C 1s XPS spectrum for Gr/Ir(111) and the graphene-covered (2x2) Dy surface alloy.

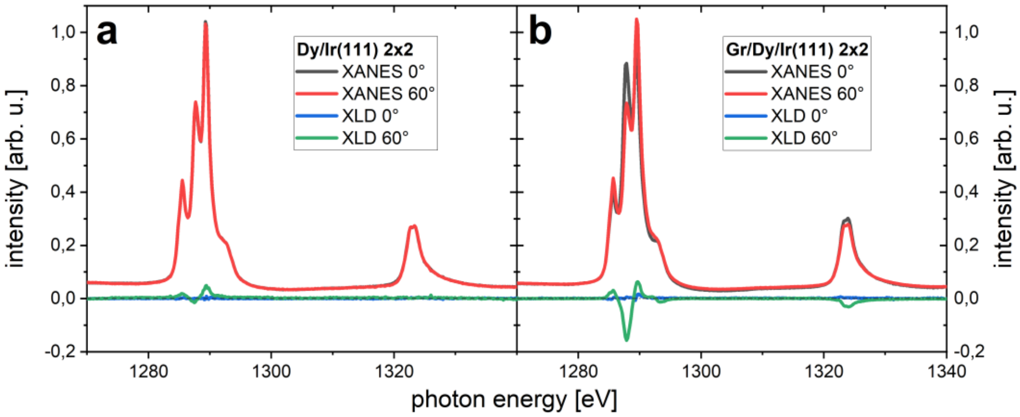

Supp. Fig. 8: Effect of graphene absorption on X-ray linear dichroism

a XANES and XLD of the (2x2) Dy surface alloy at 50 mT and 3 K for normal (0°) and grazing (60°) x-ray incidence. **b** XANES and XLD of the graphene-covered (2x2) Dy surface alloy at 50 mT and 3 K for normal (0°) and grazing (60°) x-ray incidence. The XANES spectra are shifted for better visibility.

the probed structure, X-ray linear dichroism (XLD) is the method of choice. To measure the linear dichroism, one subtracts the spectrum for linear horizontal polarized x-rays from the linear vertical one. A comparison with calculated spectra allows deeper analysis as shown in Fig. 6.

The effect of the graphene adsorption on the XLD signal is indicated in Supp. Fig. 8. As already presented in Fig. 4 a and d, the XANES shows an isotropic behaviour for the surface alloy, whereas a change is induced by the graphene adsorption, leading to an anisotropic behaviour of the XANES for the graphene-covered surface alloy. The spectra in Supp. Fig. 8 show, that this is also valid for low magnetic fields. This is also reflected in the XLD signal. While there is no effective signal expected for normal incidence due to geometric reasons, the out-of-plane component of the anisotropic charge distribution is indicated in the grazing incidence measurement. Thereby, the signal for the surface alloy is very small, while there is a strong signal for the graphene-covered surface alloy, which is analysed and discussed in detail in Fig. 6.

In the following, we are especially interested in the magnetic field dependence of the XLD signal. Other than for the surface alloy sample, where nearly no linear dichroism could be

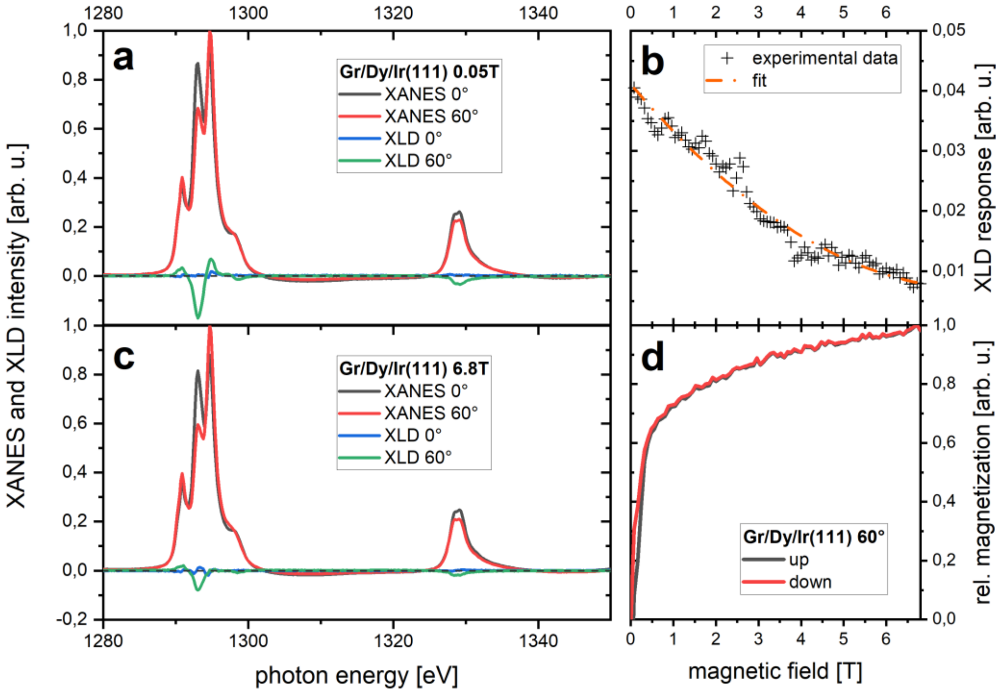

Supp. Fig. 9: Correlation between linear dichroism and magnetisation

a XANES and XLD of the graphene-covered (2x2) Dy surface alloy at zero-field for normal and grazing x-ray incidence. **b** Magnetic field dependence of XLD response of the graphene-covered (2x2) Dy surface alloy for grazing x-ray incidence. **c** XANES and XLD of the graphene-covered (2x2) Dy surface alloy at 6.8 T for normal and grazing x-ray incidence. **d** Magnetic field dependence of XMCD response of the graphene-covered (2x2) Dy surface alloy for grazing x-ray incidence.

detected, the graphene-covered surface alloy shows a clear linear dichroic signal.

In Supp. Fig. 9 a the XANES and the XLD signal of the graphene-covered surface alloy at a low magnetic field are shown. 50 mT are chosen over zero field to get a well-defined situation, as residual fields are likely present at strong superconducting magnets. The XLD signal for normal incidence is negligible, stating that there is no in-plane anisotropy. For grazing x-ray incidence, a clear dichroic signal is measured, indicating an out-of-plane charge anisotropy. Comparing this with the high-field measurement presented in Supp. Fig. 9 c, one can immediately see, that the linear dichroic signal is strongly reduced for grazing incidence, whereas there is still a negligible signal for normal incidence.

For a deeper understanding, we measured the dependence of the XLD signal on the external magnetic field. The results depicted in Supp. Fig. 9 b shows a continuous decrease of the XLD signal, indicating a continuous change of the anisotropy in the 4*f*-shell driven by the magnetic field. This shift to higher fields seems to be from the same origin as the shift of the magnetic moment to higher fields, shown in Supp. Fig. 9 d. We can explain this behaviour by the incidence and field angle of 60° to the surface normal used in the experiment due to experimental limitations. By expecting the highest magnetisation in-plane, the magnetic field forces the magnetic moment along the quantisation axis, resulting in a shift towards higher fields, as also seen in the multiplet calculation. One may think of measurements with even higher incidence angles, but a measurement parallel to the surface is obviously not possible due to geometrical reasons.

From a different view, this shows the reason for the deviation of the measured magnetic moment from Hund's rule. As stated above, the quantisation axis for our grazing incidence measurements is 60° from the surface normal. Assuming that a spin moment of 5 μ_B lies in-plane, the projected spin moment for grazing incidence would be 5 μ_B * cos(60°) = 2.5 μ_B. As the external magnetic field is aligned along the beam direction, the Dy moment is forced out of the surface plane with increasing field, leading to an increased projected moment, as clearly visible in Supp. Fig. 9 d.

multiX

Differing from other multiplet codes, multiX allows the construction of the local environment by point charges. Within this model, the relevant interactions for the electrons in the open shells are the intra-atomic electrostatic interactions, the spin-orbit coupling, and the effect of the crystal field. Considering *n* electrons in the open shells of an atom and N_{ions} point charges Q_m at position $\mathbf{R}_m$ from the atom, the multiplet Hamiltonian is given by

$$\mathcal{H}_{\text{mult}} = \sum_{i,j}^{n} \frac{e^2}{|\mathbf{r}_i - \mathbf{r}_j|} + \sum_{i}^{n} \varepsilon_i + \mathcal{V}_{\text{xtal}}.$$

The third term $\mathcal{V}_{xtal}$ is the crystal field interaction in the crystal field potential V_{xtal},

$$V_{\text{xtal}}(\mathbf{r}) = \sum_{m=1}^{N_{\text{ions}}} \frac{Q_m}{|\mathbf{r} - \mathbf{R}_m|}. \qquad (9)$$

The point charge crystal field schemes employed in the multiplet calculations are presented in Supp. Table 2 for the superstructure and Supp. Table 3 for the graphene-covered surface alloy. For both crystal fields, a scaling factor of 0.5 was used.

x (Å)	y (Å)	z (Å)	q (e)	Element
2.71	0.0	-0.67	-0.3	Ir
-2.71	0.0	-0.67	-0.3	Ir
1.355	2.346	-0.67	-0.3	Ir
1.355	-2.346	-0.67	-0.3	Ir
-1.355	2.346	-0.67	-0.3	Ir
-1.355	-2.346	-0.67	-0.3	Ir
1.01	0.586	-3.21	-0.4	Ir
-1.01	0.586	-3.21	-0.4	Ir
0.0	-1.173	-3.21	-0.4	Ir

Supp. Table 2: Crystal field parametrization for the effective ligand field of the surface alloy used to model the experimental findings (compare Fig. 5 a

x (Å)	y (Å)	z (Å)	q (e)	Element
2.71	0.0	-0.83	-0.3	Ir
-2.71	0.0	-0.83	-0.3	Ir
1.355	2.346	-0.83	-0.3	Ir
1.355	-2.346	-0.83	-0.3	Ir
-1.355	2.346	-0.83	-0.3	Ir
-1.355	-2.346	-0.83	-0.3	Ir
1.01	0.586	-3.37	-0.2	Ir
-1.01	0.586	-3.37	-0.2	Ir
0.0	-1.173	-3.37	-0.2	Ir
0.0	0.0	3.45	-0.195	C
1.42	0.0	3.45	-0.195	C
-0.71	1.23	3.45	-0.195	C
-0.71	-1.23	3.45	-0.195	C

Supp. Table 3: Crystal field parametrization for the effective ligand field of the graphene-covered (2x2) Dy surface alloy used to model the experimental findings (compare Fig. 5 b)

Notes and references

1 Carra, P. et al. X-ray circular dichroism and local magnetic fields. Physical Review Letters 70, 5 (1993).

2 Collins, S. P. et al. An investigation of uranium M4,5 edge magnetic X-ray circular dichroism in US. *Journal of Physics: Condensed Matter* **7**, 48 (1995).

3 Friedrich, R. et al. Exchange interactions of magnetic surfaces below two-dimensional materials. *Physical Review B* **93**, 22 (2016).

4 Callsen, M. et al. Magnetic hardening induced by nonmagnetic organic molecules. *Physical Review Letters* **111**, 10 (2013).

5 Friedrich, R. et al. Molecular induced skyhook effect for magnetic interlayer softening. *Physical Review B* **92**, 19 (2015)

6 Raman, K. et al. Interface-engineered templates for molecular spin memory devices. *Nature* **493**, 7433 (2013).

7 Brede, J. et al. Long-range magnetic coupling between nanoscale organic-metal hybrids mediated by a nanoskyrmion lattice. Nature Nanotechnology 9, 12 (2014).
8 Schröder, U. A. et al. Core level shifts of intercalated graphene. 2D Materials 4, 1 (2017).
9 Uldry, A.; Vernay, F. & Delley, B. Systematic computation of crystal-field multiplets for x-ray core spectroscopies. Physical Review B 85, 12 (2012).